Final Report

1. DOE award # and name of the recipient

Award #: DOE DE-SC0008684
Recipient: Stanford University

2. Project Title and name of the PI

Project title: Densely Aligned Graphene Nanoribbon Arrays and Bandgap Engineering
PI: Hongjie Dai

3. Date of the report and period covered by the report

Date of report: 01/04/2017
Period covered 09/01/2012 – 11/30/2016

4. Research accomplishments.

4.1 Project Objectives.

Project Objective 1:
Develop novel approach to ~5-20 nm wide aligned GNRs in parallel arrays with high density (pitch 30-50nm), smooth edges and pre-defined edge orientation.
Final Report: We have achieved this goal using a novel block copolymer based etching mask to pattern graphene into dense GNR arrays.

Project objective 2:
Graphene bandgap engineering. We plan to apply uniaxial strain to individual and arrays of GNRs and quantify the bandgaps through electrical transport measurements.
Final Report: We have succeeded in tuning the electrical properties of single GNRs by strain.

Project Objective 3:
Micro-Raman spectroscopy to understand the properties of GNRs under uniaxial strain. We are aimed at using micro-Raman spectroscopy to accurately measure the strains in GNRs on flexible substrates.
Final Report: We have succeeded in performing raman spectroscopy of single GNR while tuning its electrical properties by strain.

Project Objective 4:
Parallel dense GNR arrays for field effect transistors. We are aimed at high performance GNR FETs with high on/off ratios and high on-state currents.
Final Report: We have succeeded in building high performance FETs based on massively parallel purified single walled carbon nanotubes.

4.2 Results.

Project 1 Results:

Fabrication of free standing nano-masks by self-assembled diblock copolymer films

We developed a process by spin-coating poly(styrene-b-dimethylsiloxane) (PS-PDMS) on thin Au film covered SiO_2/Si substrate (Figure 1). Then the PS-PDMS/Au/SiO_2/Si substrate was annealed in benzene vapor at room temperature for self-assembly of the PS-PDMS block-copolymer into line patterns. After that, O_2 plasma was used to etch the PS block away while the oxidized PDMS lines (SiO_x lines) will remain. Then the substrate was put in hot KOH to separate oxidized-PDMS/Au from SiO_2/Si. The Au film was then be etched by KI-I_2 solution, leaving the oxidized PDMS (SiO_x) lines forming the free standing nano-mask. This approach produced ultra-dense, well aligned SiO_x lines as masks useful for patterning a wide range of materials including graphene.

Free standing nano-mask patterning of dense aligned GNR arrays

The SiO_x line pattern direction of the free standing nano-mask was placed on top of the graphene sample. Plasma etching was performed to etching the graphene regions not covered by the SiO_x lines in the nano- mask, yielding parallel GNR arrays with pitch down to the tens of nm regime. This led to ultradense GNR arrays. This work was published in Nano Research.

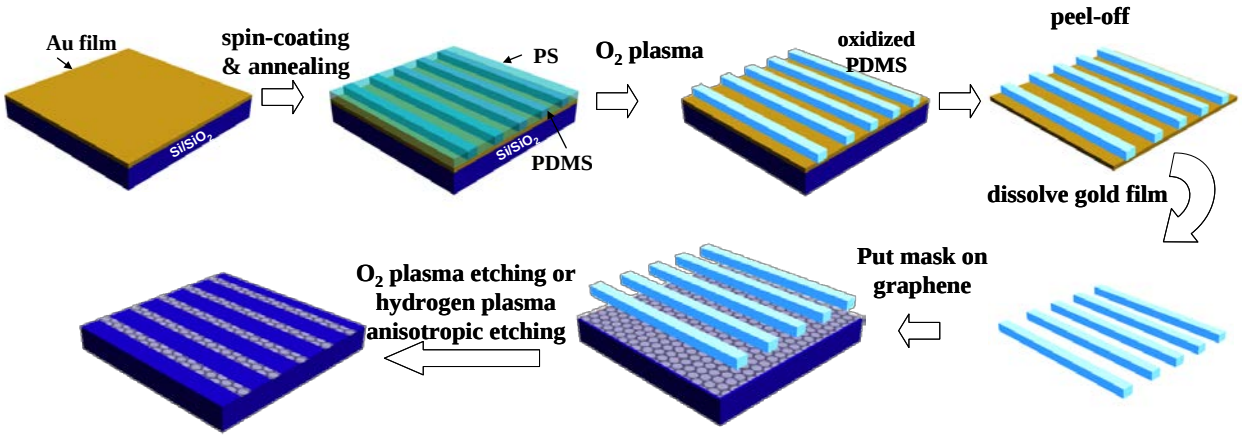

Figure 1. Schematic approach to making parallel aligned GNR arrays by dry etching through a free standing nano-mask formed by self assembled poly(styrene-b-dimethylsiloxane) (PS-PDMS) diblock copolymer.

Project 2 & 3 Results:

Strain graphene nanoribbons by AFM manipulation for bandgap engineering

The objectives are GNR bandgap engineering by uniaxial strain and characterizations by electrical measurements of the on/off ratios of GNR devices, micro-Raman spectroscopy to investigate edge structures and the properties of GNRs under uniaxial strain and parallel dense GNR arrays for field effect transistors.

One of the major hurdles to practical graphene electronics is the lack of a bandgap within the bulk material. Confinement in the lateral direction by forming nanoribbons is one

possible solution; however the production of GNRs with smooth edges at very narrow widths <10nm has proven elusive. Theoretical calculations demonstrate that uniaxial strain can change the bandgap depending on the ribbon's edge chirality. For certain edge types and widths, straining the GNR should produce an increase in the bandgap.

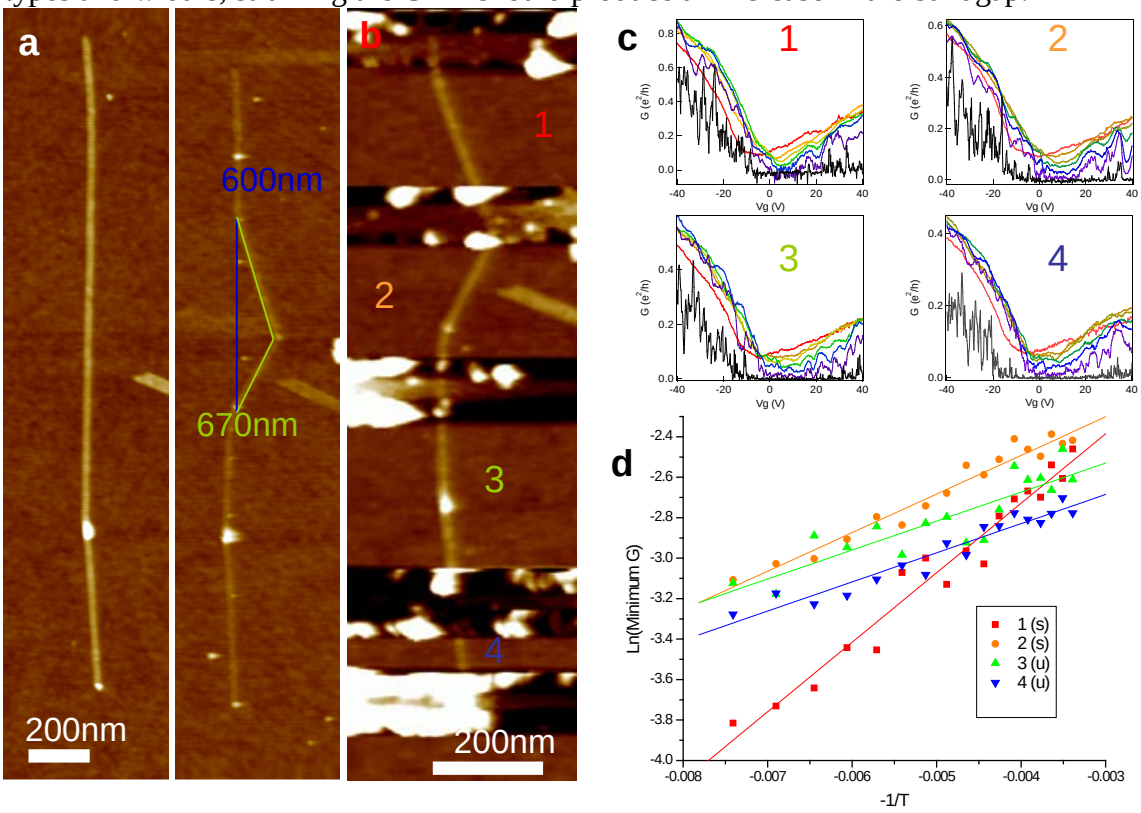

Figure 2 (a) AFM image of a GNR before and after bending. (b) AFM image of device made from bent GNR. Sections 1 and 2 include the strained area of the GNR. (c) Source-drain current vs. back gate voltage (I_d-V_{gs}) characteristics of FETs made on GNR sections at 1mV bias. Numbers correspond to section labeling in (b). Curves were taken from 295K to 5K, colored red through black (red corresponds to 295K). (d) Arrhenius plots of the minimum conductance point of all four devices, color coded to same sections as in (b) and (c). Estimating the bandgaps using the slope of the Arrhenius plot produces the values of 59, 32, 25, 25 meV for sections 1-4 respectively.

We have succeeded in straining individual GNRs. We use an AFM tip to move the GNR, forming a triangle in the middle while the ends of the GNR remain stationary due to friction (Figure 2). As the total length of the GNR has increased, there should be a uniaxial strain primarily on the lengths of the GNR that form the sides of the triangle. By fabricating FETs on the GNRs' different sections, the bandgap can be found via low temperature measurements, demonstrating the bandgap's dependence on strain. Variations on the experiment, including bending the GNR after device fabrication and after low temperature measurements were also performed to ensure that the strain was the cause of the effect. Evidence of both increasing and decreasing bandgap, and similar variation in on/off ratio, was found to result from the strain (Figure 2).

Raman spectroscopy of GNRs under strain.

We study strain in single GNRs via Raman spectroscopy, and we find a linear relationship between strain and G band peak location (Figure 4). The G band in GNRs show an approximate linear dependence on uniaxial strain with downshifts under strain at a rate of about -10 cm^{-1} per 1% strain. The linear relationship matches theoretical predictions on the E_{2g} phonon and its shift in energy with strain. Our shift is lower than theoretical values, likely due to substrate interaction that could not be modeled in the simulation.

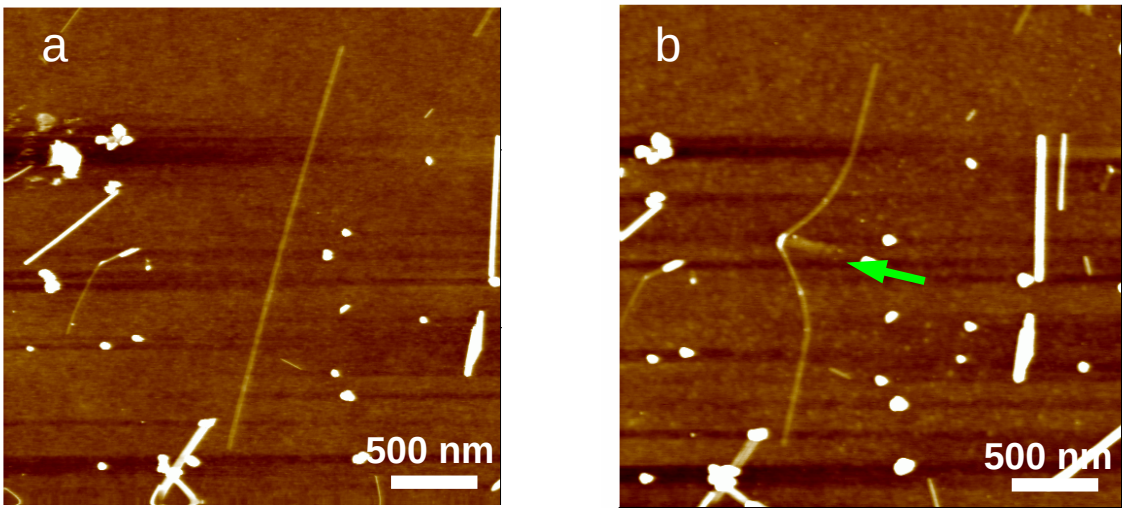

Figure 3: The straining of a GNR (GNR 1) by the AFM manipulation. (a) AFM image of the GNR 1 coated by the PmPV before AFM manipulation. (b) AFM image of the GNR 1 manipulated and then calcined to remove the PmPV; the arrow shows the direction of the AFM tip pushing the GNR. The GNR is 26 nm in width and 1.2 nm in height.

Strained graphene nanoribbons characterized by Raman and electrical transport.

For the same GNRs, we have done Raman studies and performed low temperature measurements and NEGF simulation of the electrical properties and the bandgap along different segments of the ribbon (Figure 4,5). It was found that the shift of the GNR's G bands had an approximately linear dependence on the uniaxial strain, with shift rates estimated to be -10.3 cm^{-1}/% and -8.7 cm^{-1}/% for two strained GNRs respectively. We investigated theoretically the G band's shift as a function of uniaxial strain for GNRs of various widths. The shift of Raman G band of strained graphene was due to shifting of

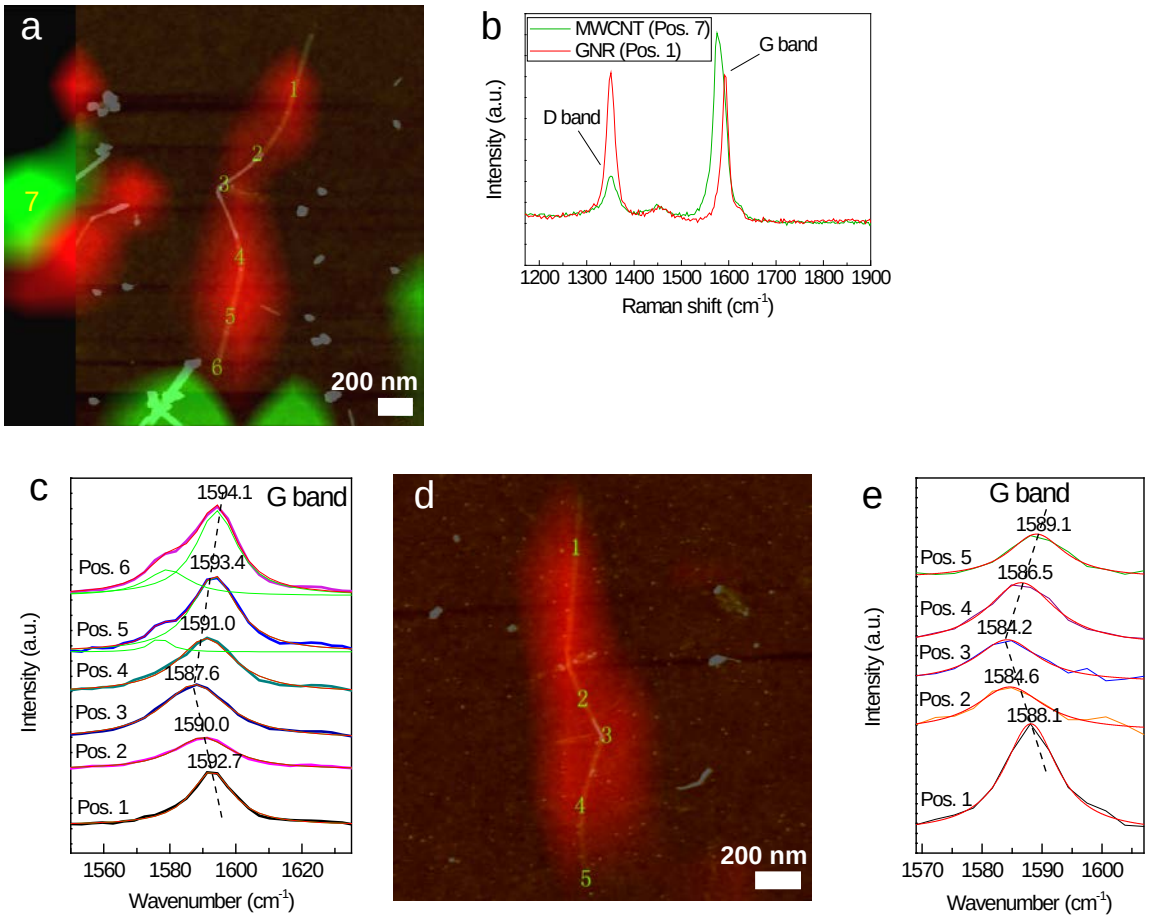

Figure 4: Raman mapping and spectra of strained GNRs. (a) An overlay of the Raman image and the AFM image for the strained GNR 1; The Raman image is plotted by the combined intensity integral in the D-band 1324-1360 cm^{-1} region (red) and G-band 1559-1592 cm^{-1} region (green) to show the GNR and the MWCNT in different color. (b) Raman spectra at the position 1 and 7 in (a), showing the typical Raman spectra for the GNR and CNT, respectively. (c) The Raman spectra taken along the strained GNR 1. The spectra are fitted with Lorentzians (red and green fitting lines) to obtain the peak positions of G bands, showing a gradual downshift of the G band from the end position to the manipulated position in the GNR; The spectra at position 1 to 4 are fitted with single peak and the spectra at position 5, 6 are fitted with two peaks (the lower fitted peak derives from the MWCNT nearby). (d) Raman spectra including both D and G bands at the position 1 and 3 in (a). (e) An overlay of the Raman image and the AFM image for the strained GNR 2; The Raman image is generated from the intensity integral of the D band in the 1339-1366 cm^{-1} region (red). (f) The Raman spectra taken along the strained GNR 2; the spectra are fitted (red fitting lines) to obtain the peak positions of G bands.

the optical phonon (OP) mode, and the shift of the G band under uniaxial strain for different widths of armchair GNRs (denoted with the number of dimer lines N_a across the ribbon with N_a=7, 10, 22 and 28) and 2D graphene was then extracted. It was observed that the theoretical G band's shift increased linearly with the increase of the uniaxial

strain for various widths of GNRs, consistent with the experimental result. Calculations showed that the layer number and edge chirality of the GNR did not have an obvious effect on the shift rate of the G band under uniaxial strain. We found that the shift rate of the G band decreased with the width of the GNR, and the smaller shift rates for narrower GNRs were due to the effect of GNR edges which modified the force constant of GNRs.

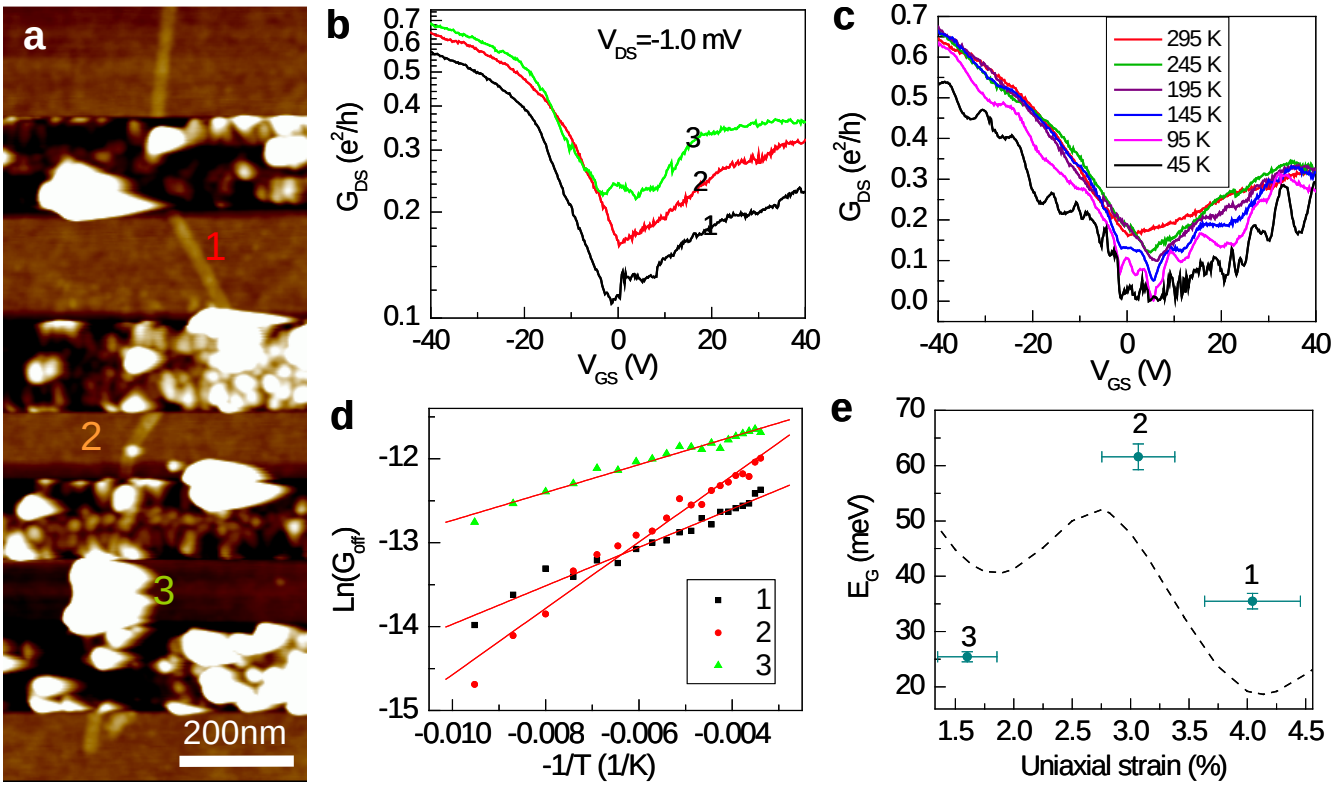

Figure 5. Electrical characteristics of strained GNRs. (a) An AFM image of three three-terminal FET devices on SiO_2/Si (with Si back gate) fabricated along strained 19-nm-wide GNR 3. The three GNR segments labeled as 1, 2 and 3 have strains of 4.04±0.41%, 3.07±0.31% and 1.60±0.25% respectively, as estimated from the midpoint of the segments and the variation in strain along the segments. (b) Room-temperature conductance as a function of gate bias (G_{DS}-V_{GS}) of the three GNR segments. (c) Temperature-dependent G_{DS}-V_{GS} curves of FET 2 at drain bias V_{DS}= -1.0 mV. (d) The minimum conductance of G_{DS}-V_{GS} curves for the three devices as a function of the inverse of temperature from 295 K to 105 K at intervals of 10 K. The red lines are the linear fit to the experimental data. (e) Extracted experimental bandgaps under each uniaxial strain of the three segments. Horizontal error bars cover the range of strain in each channel; Vertical error bars show the fitting error of the bandgap extraction. The dash line in the figure shows the theoretical bandgap of a 19-nm-wide (9,6) chiral GNR, to show the expected bandgap change and strain modulation behavior for similar width of GNR.

To investigate the electrical properties of strained GNRs, we made field-effect transistors (FETs) on individual strained GNRs by e-beam lithography and lift-off with palladium (Pd) used as the source and drain contacts. For GNRFETs fabricated on a strained 19-nm-wide monolayer GNR (GNR 3) (**Figure 5**a), the strains of the three GNR segments

(labeled 1-3 in Figure 5a) were about 4.04%, 3.07% and 1.60% respectively estimated from the midpoint of the segments. Room-temperature electrical characteristics and temperature-dependent measurements (Figure 5b and 5c respectively) for these GNRFETs showed an increase in the on/off current ratio in the transfer characteristic curves at lower temperatures, with a decrease in the minimum conductance by more than 2 orders of magnitude from *295 K* to *45 K* for the FET 2 as shown in Figure 5c. A plot of the minimum conductance (G_{off}) as a function of inverse temperature, $\ln(G_{off}) \propto T^{-1}$ (Figure 6d) showed a linear relation in the temperature range of 295 K to 105 K, corresponding to conductance primarily through thermally activated carriers at the point of minimum conductance. We performed non-equilibrium Green's function (NEGF) simulation to fit the asymmetric transfer characteristics and extracted the bandgap of GNRs (E_g) of ~35, ~62 and ~25 meV for segments 1, 2 and 3 of the strained GNR (with strains of about 4.04%, 3.07% and 1.60%) respectively (see Figure 5e). It was shown that the uniaxial tensile strain could effectively modulate the GNR bandgap, which was altered by about 2.5 times from 25 meV to 62 meV that was measured at the different segment with different strain. A similar non-monotonic varying trend of the bandgaps was observed for all of our 8 measured strained GNRs with widths ranging from ~17 to ~26 nm.

We simulated the bandgap dependence on uniaxial strain for various chiralities of GNRs using the p_z orbital tight-binding model. For a calculated 19-nm-wide (9,6) GNR, a non-monotonic fluctuating bandgap change was observed, with a similar period and amplitude of the bandgap variation under uniaxial strain as seen in the experimental result (Figure 5e). The further calculations showed that the bandgap of a similar width of armchair GNR as a function of uniaxial strain had an oscillatory dependence while that of the similar width of zigzag GNR displayed minute monotonic increase under uniaxial strain.

Simulation of armchair GNRs showed that the bandgap will be increased from ~215 meV to ~400 meV when the uniaxial strain varies from 0% to 2.0% for a 4.3-nm-wide ribbon. A bandgap of 400 meV could afford an on/off ratio of 10^6 to 10^7 for a Pd-contacted p-type unipolar GNRFET, which could be used in complementary metal-oxide-semiconductor (CMOS) logic devices. As a reference, a 2.0-nm-wide unstrained GNR would exhibit a similar bandgap of ~410 meV. Therefore, with a suitable uniaxial strain applied to armchair GNRs, the GNR's width restriction for logic application can be relaxed to a larger range up to ~5 nm rather than sub-2 nm. Theoretical simulations had predicted that the impact of the scattering induced by line-edge roughness (LER) rapidly degraded mobility for ribbon widths less than 5 nm. Towards this direction, a chemical synthesis method that can reliably produce high-quality GNRs with controlled width ~5 nm will be expected for future high-performance strained-GNR logic device application.

To summarize this project, uniaxial strain has been successfully introduced into individual GNRs for the first time by AFM manipulation to investigate effects of strain on the Raman spectroscopic and electrical properties of GNRs. It was found that the Raman G-band frequency of GNRs downshifted linearly under uniaxial strain at a shift rate of about -10 cm^{-1}/% for GNRs with a width of around 20 nm. The bandgap of GNRs could be tuned significantly by uniaxial strain in a non-monotonic fluctuating way,

varying from 25 to 62 meV for a 19-nm-wide GNR under strain. Theoretical modelings on the Raman G-band shift and bandgap variation of GNRs under uniaxial strains was also performed, showing good agreement with the experimental results. Strain engineering of GNRs opens a path to tune the bandgap of graphene and is promising for tailoring the properties of GNRs towards versatile electronics and photonics applications. This work has been published in **Adv. Mater.**

Project 4 Results: Functional FET devices with parallel GNRs.

Dense aligned carbon nanotube assembly

One of the approaches to densely aligned GNRs that we will pursue is to unzip or collapse densely aligned carbon nanotubes (CNTs) to transform them into dense aligned GNRs. Through the program, we realized that GNRs might not be as good as CNTs for electronics because of the difficulty in developing a robust bandgap, large enough for FETs. Therefore, we have pursued both aligned GNRs and CNTs and compare their electrical properties and device performances. The hurdles to practical carbon nanotube electronics include metal vs. semiconducting nanotube sorting, and assembly of the sorted nanotubes into ordered structures. We have developed a method of achieving self-assembly of semiconducting single-walled carbon nanotubes (s-SWNTs) into densely aligned rafts (Figure 6).

We separated purely semiconducting SWNTs from bulk materials and assembled them into densely aligned 2D rafts using depletion attraction forces between suspended nanotubes. Characterization by microscopy and spectroscopy revealed a high degree of alignment and an unprecedented packing density of ~100 SWNTs/μm in the highly aligned, densely packed 2D rafts of semiconducting tubes. Field-effect transistors (FETs) made from aligned SWNT rafts afforded short channel (~150 nm long) devices comprised of tens of purely semiconducting SWNTs derived from chemical separation within a < 1 μm channel width, achieving unprecedented high on-currents (up to ~120 μA per device) with high on/off ratios.

Using this raft method to densely pack SWNTs locally allows for a much higher current and current density for SWNT FETs than has been previously reported. Our ability to pack SWNTs so closely together in a 2D fashion while maintaining a high current per SWNT solves a local density problem that has been difficult to solve due to the high aspect ratio and surface energy of the SWNTs. Previous solutions have either been limited in density or in current per SWNT. Our method approaches the problem of future integrated CNT circuits from a new direction in its focus on CNT proximity while maintaining high current, and consequently makes progress in current and current density.

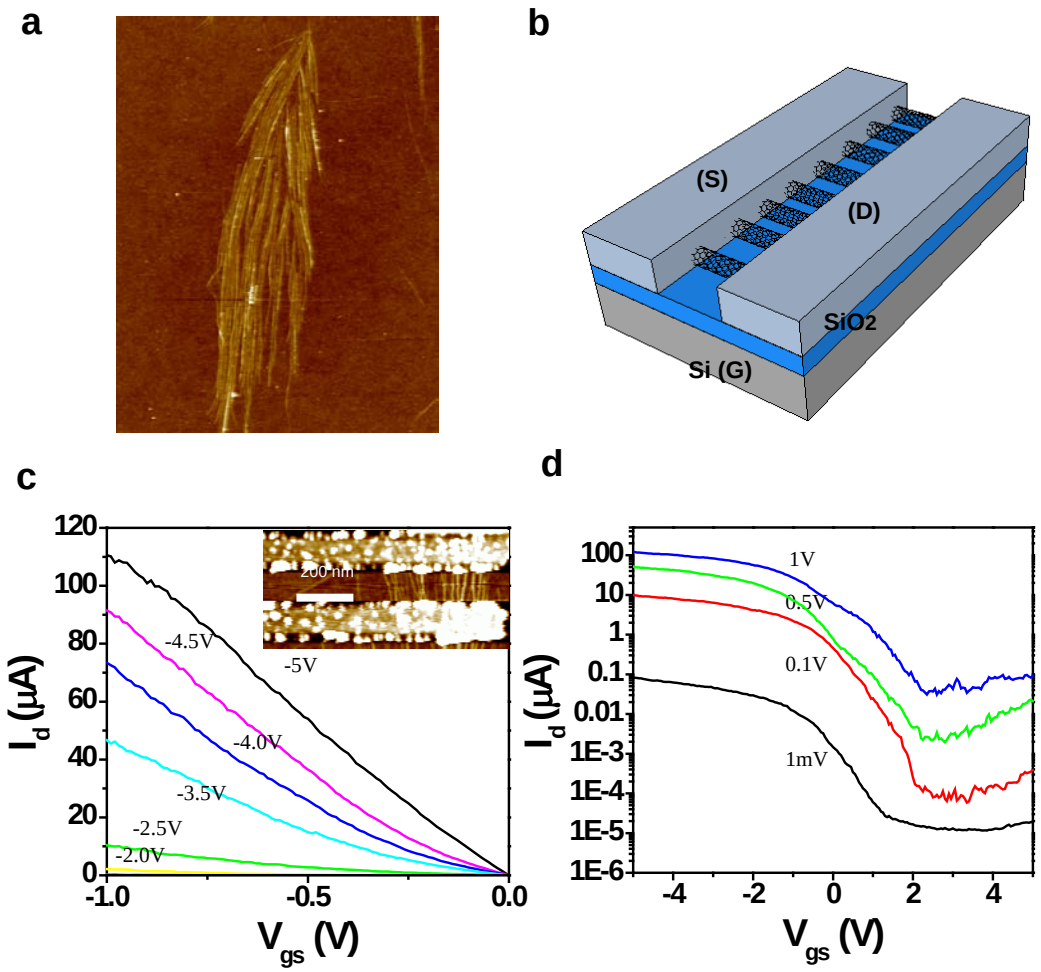

Figure 6 (a) AFM image of a s-SWNT raft. (b) Schematic of short channel device on 10 nm SiO_2 (c) Source-drain current vs. back gate voltage (I_d-V_{gs}) characteristics of FET made on s-SWNTs raft with a channel length of 140nm. Bias voltages: 1 V, 500 mV, 100 mV and 1mV, from top to bottom. (d) I_d-V_{ds} curves of the same FET as in (c)

Patterning of densely aligned carbon nanotube assembly

The raft self-assembly of semiconducting single-walled carbon nanotubes (s-SWNTs) above was randomly formed on a substrate. Next, we further developed this process by achieving positional control of these rafts, and depositing them into densely pitched lithographically defined channels.

Highly pure semiconducting SWNTs are self-assembled using depletion attraction forces into rafts along lithographically defined patterns of narrow pitch of 100 and 200nm (Fig. 7). These rafts consist of individual CNTs and thin bundles of a few CNTs densely packed in the plane of the substrate. Characterization by microscopy and spectroscopy revealed a high degree of fidelity of the assembled dense SWNT structures to the lithographically defined pattern. Up to 97% of 0.1 mm channel lengths were densely

packed with SWNTs at densities up to 80 SWNTs/µm. Field-effect transistors (FETs) made from these arrays exhibited high performance, with devices showing current density of ~100 µA/µm and a total current of 84 µA/device at on/off ratios > 1000 (Fig. 7,8).

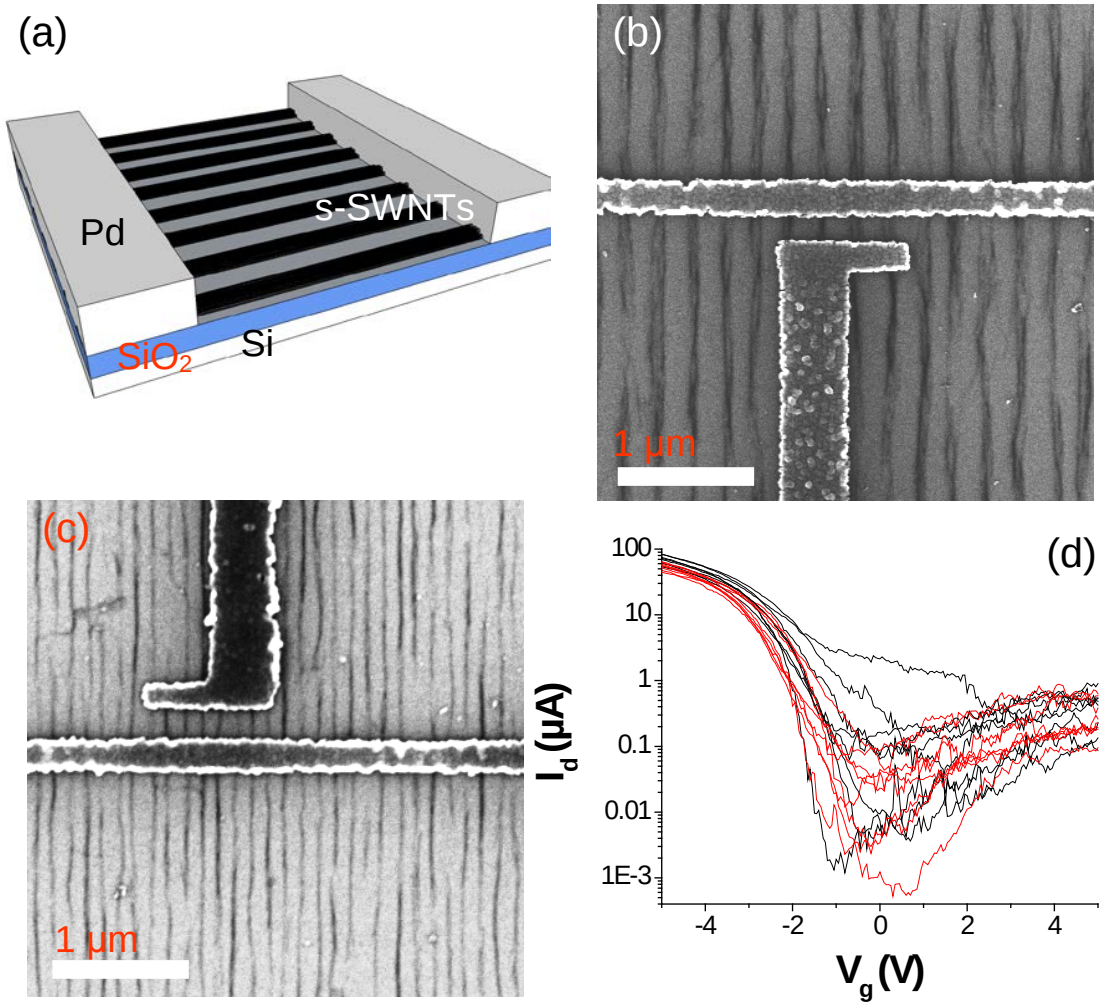

Figure 7: a) Schematic of SWNT FET structure. b-c) SEM images of fabricated FETs on patterned rafts. d) Id-Vg curves of depletable raft FETs measured. 100nm pitch FETs in red, 200nm pitch FETs in black.

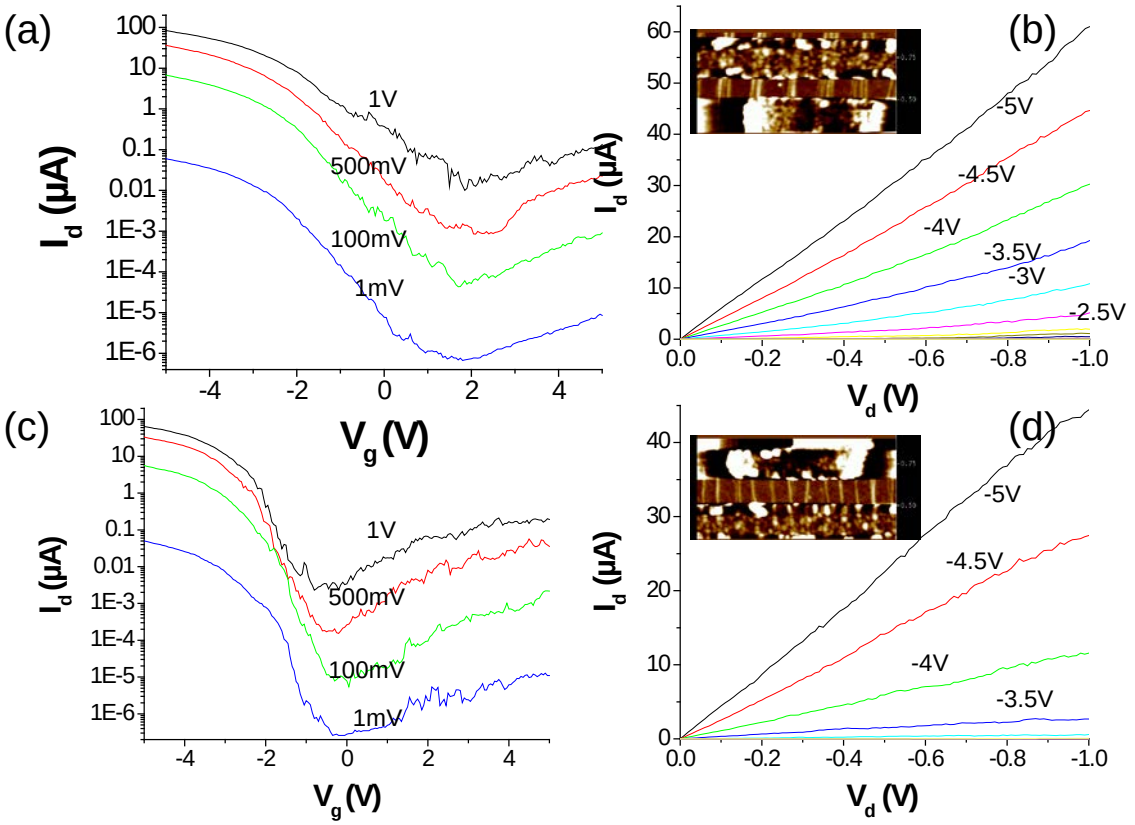

Figure 8: a) Id-Vg curves of highest current raft FET with 200nm pitch patterning at 1000, 500, 100, 1 mV biases. b) Id-Vd curves of device shown in (a). c) Id-Vg curves of highest current raft FET with 100nm pitch patterning at 1000, 500, 100, 1 mV biases. d) Id-Vd curves of device shown in (c).

Using this raft method to densely pack SWNTs locally allows for a much higher current and current density for SWNT FETs. Our process provides the highest on current and current density of SWNTs structures deposited in lithographically defined patterns. Previous solutions have either been limited in density or in current per SWNT. Our method approaches the problem of future integrated CNT circuits from a new direction in its focus on CNT proximity in lithographically defined areas while maintaining high current per CNT, and consequently makes progress in current and current density.

Additional Results:

We have leveraged this grant to research in the area of developing novel carbon nanomaterials for renewable energy applications, and the publications have acknowledged funding by this grant.

Water splitting with novel electrocatalysts using a single AAA battery.
Hydrogen, as a clean and renewable energy resource, has been intensely investigated as an alternative to the diminishing fossil fuel. An effective way of producing high purity hydrogen is to electrochemically split water into hydrogen and oxygen in an electrolyzer. The state-of-art hydrogen evolution HER catalyst is platinum (Pt) and its alloys, but the scarcity and cost of Pt limit its large-scale application for electrolysis. It have been difficult to achieve both high activity and stability matching those of Pt. For oxygen evolution OER catalyst, Ir metal is the most active but is also expensive and not stable.

Recently we developed a nickel oxide/nickel (NiO/Ni) hetero-junction like structure attached to mildly oxidized carbon nanotube (NiO/Ni-CNT) exhibiting high HER catalytic activity close to commercial Pt/C catalysts in several types of basic solutions (pH=9.5-14). The high catalytic activity of NiO/Ni-CNT towards HER enabled a high performance electrolyzer with ~20 mA cm^{-2} at a voltage of 1.5 V, which sets a low voltage record for water electrolysis using non-precious metal catalysts. This work leveraged our nanotube research in the DOE project, and was published in **Nature Communications**.

An ultrafast rechargeable aluminum ion battery.
The development of new rechargeable battery systems could fuel various energy applications from personal electronics to grid storage. Due to the low cost, low flammability and 3-electron redox properties of aluminum, rechargeable Al-based batteries could offer cost-effectiveness, high capacity and safety, leading to a breakthrough in energy storage technology. However, rechargeable Al battery research over the past 30 years has failed to compete with other battery systems. These efforts have been plagued by problems such as cathode material disintegration, low cell discharge voltage (~0.55 V), capacitive behavior without discharge voltage plateaus (1.1–0.2 V or 1.8–0.8 V), and insufficient cycle life (<100 cycles) with rapid capacity decay (by 26%–85% over 100 cycles).

We made a breakthrough recently by developing a high-performance rechargeable aluminum battery with high-rate capability using an aluminum (Al) metal anode and novel graphitic materials for the cathode. The battery operates through electrochemical deposition/dissolution of Al and intercalation/de-intercalation of chloroaluminate anions in graphite using a safe, non-flammable ionic liquid electrolyte. The cell exhibited well-defined discharge voltage plateaus near ~2 V, a specific capacity ~70 mAh g^{-1} and ~98% Coulombic efficiency. A novel three-dimensional (3D) graphitic foam cathode was found to enable fast anion diffusion and intercalation, affording unprecedented charging times (~1 minute) with high current densities ~4,000 mA g^{-1} (~ 3,000 W kg^{-1}), which can

withstand > 7,500 cycles without capacity decay. The aluminum battery has the potential for cost effectiveness, high safety and high charging speed, making it a promising new energy storage system. This work was published in **Nature** and generated significant interest.

5. A list of publications

All papers below have DOE support acknowledged

Justin Wu, Liying Jiao, Alexander Antaris, Charina L. Choi, Liming Xie, Yingpeng Wu, Shuo Diao, Changxin Chen, Yongsheng Chen, and Dai. "Self-Assembly of Semiconducting Single-Walled Carbon Nanotubes into Dense, Aligned Rafts" ***Small,*** 9 (24), 4142-4142, 2013.

Changxin Chen, Justin Zachary Wu1, Kai Tak Lam, Guosong Hong, Ming Gong, Bo Zhang, Yang Lu, Alexander L. Antaris, Shuo Diao, Jing Guo and Dai. "Graphene Nanoribbons Under Mechanical Strain" ***Advanced Materials***, 5, 4070-4075, 2014.

Justin Wu, Alexander Antaris, Ming Gong, and Dai. "Top-Down Patterning and Self-Assembly for Regular Arrays of Semiconducting Single-Walled Carbon Nanotubes" ***Advanced Materials***, 26, 6151-6156, 2014.

Ming Gong, Wu Zhou, Mon-Che Tsai, Jigang Zhou, Mingyun Guan, Meng-Chang Lin, Bo Zhang, Yongfeng Hu, Di-Yan Wang, Jiang Yang, Stephen J. Pennycook, Bing-Joe Hwang, and Dai. "Nanoscale nickel oxide/nickel heterostructures for active hydrogen evolution electrocatalysis" **Nature Communications**, 5 4695, 2014.

Ming Gong, WuZhou, Michael James Kenney, RichKapusta, Sam Cowley, Yingpeng Wu, Bingan Lu, Meng-Chang Lin, Di-Yan Wang, Jiang Yang, Bing-Joe Hwang, and Dai. "Blending Cr2O3 into a NiO Ni Electrocatalyst for Sustained Water Splitting" ***Angewandte Chemie***, 127, 12157-12161, 2015.

Liying Jiao, Liming Xie and Hongjie Dai. "Densely aligned graphene nanoribbons at 35 nm pitch."***Nano Research.*** 5, 292-296, 2012.

Meng-Chang Lin, Ming Gong, Bingan Lu, Yingpeng Wu, Di-Yan Wang, Mingyun Guan, Michael Angell, Changxin Chen, Jiang Yang, Bing-Joe Hwang, and Dai. "An ultrafast rechargeable aluminium-ion battery" ***Nature***, 520, 324-328, 2015.

Ming Gong, Yanguang Li, Hailiang Wang, Yongye Liang, Justin Z. Wu, Jigang Zhou, Jian Wang, Tom Regier, Fei Wei, and Dai. "An Advanced Ni Fe Layered Double Hydroxide Electrocatalyst for Water Oxidation" ***JACS,*** 135 (23) 8452-8455, 2013.

6. A list of people worked on the project -graduate students, postdocs, visitors, technicians, etc. Indicate for each whether receiving full or partial support. In case of partial support indicate percentage of support.

Graduate student: Justin Wu, full support. Ming Gong: contributor.

Postdoc: Changxin Chen, full support.

Postdoc: Charina Choi, Mengchang Lin, contributors.